Measurements of R for e^+e^- annihilation at the KEK collider TRISTAN

T. Kumita,[a] H. Sagawa,[b] P. Auchincloss,[a] D. Blanis,[a] A. Bodek,[a] H. Budd,[a] S. Eno,[a] C. A. Fry,[a,b] H. Harada,[a] Y. H. Ho,[a] Y. K. Kim,[a] T. Mori,[a] S. L. Olsen,[a,i] N. M. Shaw,[a] A. Sill,[a] E. H. Thorndike,[a] K. Ueno,[a] H. W. Zheng,[a] K. Abe,[b] Y. Fujii,[b] Y. Higashi,[b] S. K. Kim,[b] Y. Kurihara,[b] A. Maki,[b] T. Nozaki,[b] T. Omori,[b] Y. Sakai,[b] Y. Sugimoto,[b] Y. Takaiwa,[b] S. Terada,[b] R. Walker,[b,a] R. Imlay,[c] P. Kirk,[c] J. Lim,[c] R. R. McNeil,[c] W. Metcalf,[c] S. S. Myung,[c] C. P. Cheng,[d] P. Gu,[d] J. Li,[d] Y. K. Li,[d,f] M. H. Ye,[d] Y. C. Zhu,[d] A. Abashian,[e] K. Gotow,[e] K. P. Hu,[e] E. H. Low,[e] M. E. Mattson,[e] L. Piilonen,[e] K. L. Sterner,[e] S. Lusin,[f] C. Rosenfeld,[f] A. T. M. Wang,[f] S. Wilson,[f] M. Frautschi,[g] H. Kagan,[g] R. Kass,[g] C. G. Trahern,[g] R. E. Breedon,[h,b] G. N. Kim,[h,b] Winston Ko,[h] R. L. Lander,[h] K. Maeshima,[h] R. L. Malchow,[h] J. R. Smith,[h] D. Stuart,[h] F. Kajino,[j] D. Perticone,[k] R. Poling,[k] T. Thomas,[k] Y. Ishi,[l] K. Miyano,[l] H. Miyata,[l] T. Sasaki,[l] Y. Yamashita,[m] A. Bacala,[n,o] J. Liu,[n] I. H. Park,[n] F. Sannes,[n] S. Schnetzer,[n] R. Stone,[n] J. Vinson,[n] S. Kobayashi,[p] A. Murakami,[p] J. S. Kang,[q] H. J. Kim,[q] M. H. Lee,[q] D. H. Han,[r] E. J. Kim,[r] D. Son,[r] T. Kojima,[s] S. Matsumoto,[s] R. Tanaka,[s] Y. Yamagishi,[s] T. Yasuda,[s] T. Ishizuka,[t] and K. Ohta[t]

[a] *University of Rochester, Rochester, New York 14627*
[b] *KEK, National Laboratory for High Energy Physics, Ibaraki 305*
[c] *Louisiana State University, Baton Rouge, Louisiana 70803*
[d] *Institute of High Energy Physics, Beijing 100039*
[e] *Virginia Polytechnic Institute and State University, Blacksburg, Virginia 24061*
[f] *University of South Carolina, Columbia, South Carolina 29208*
[g] *Ohio State University, Columbus, Ohio 43210*
[h] *University of California, Davis, California 95616*
[i] *Tsukuba University, Ibaraki 305*
[j] *Konan University, Kobe 658*
[k] *University of Minnesota, Minneapolis, Minnesota 55455*
[l] *Niigata University, Niigata 950-21*
[m] *Nihon Dental College, Niigata 951*
[n] *Rutgers University, Piscataway, New Jersey 08854*
[o] *University of the Philippines, Quezon City, 3004*
[p] *Saga University, Saga 840*
[q] *Korea University, Seoul 136-701*
[r] *Kyungpook National University, Taegu 702-701*
[s] *Chuo University, Tokyo 112*
[t] *Saitama University, Urawa 338*

(The AMY Collaboration)

(Received 5 February 1990)

The ratio R of the total cross section for e^+e^- annihilation into hadrons to the lowest-order QED cross section for $e^+e^-\to\mu^+\mu^-$ has been measured for center-of-mass energies ranging from 50 to 61.4 GeV. If we allow for an overall shift of -4.9%, about 1.5 times our estimated normalization error, the results are consistent with the standard-model predictions.

I. INTRODUCTION

In the standard model (SM) the process of electron-positron annihilation into multihadron final states proceeds by the production of pointlike quark-antiquark ($q\bar{q}$) pairs that subsequently hadronize into physically observable particles. Since the total cross section for this process is independent of the poorly understood hadronization process, it is particularly useful for providing unambiguous tests of the model's predictions. In this paper we report measurements of the total cross section for e^+e^- annihilation into hadrons for the center-of-mass energy range $50\le\sqrt{s}\le61.4$ GeV, using the AMY detector at the TRISTAN storage ring at the Japan National Laboratory for High Energy Physics (KEK). The results for $\sqrt{s}\le57$ GeV have been previously reported elsewhere.[1,2]

The lowest-order diagram for the process $e^+e^-\to q\bar{q}$, shown in Fig. 1(a), differs from that for dimuon production $e^+e^-\to\mu^+\mu^-$ [Fig. 1(b)], only in the relative

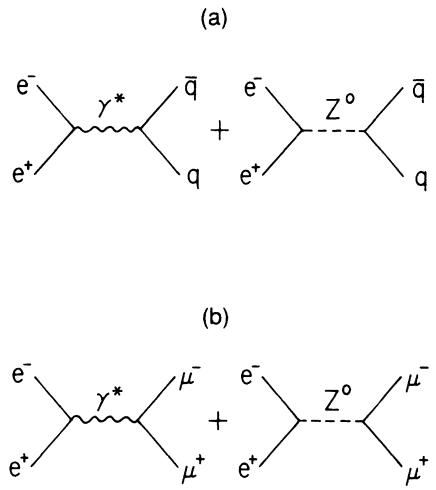

FIG. 1. (a) The lowest-order diagram for the process $e^+e^-\to q\bar{q}$. (b) The lowest-order diagram for the process $e^+e^-\to\mu^+\mu^-$.

charges of the quarks and muons. Thus, it is customary to report cross-section measurements in terms of the ratio R, which is the total multihadron annihilation cross section divided by $4\pi\alpha^2/3s$, the lowest-order QED term for dimuon production. The original quark-parton model predicts R to be simply $3\sum e_q^2$, where the factor of 3 reflects the three color states of each quark flavor, e_q is the quark charge in units of the electron charge, and the sum is over all quark flavors. When the five observed quark flavors are included, this expression evaluates to $R=\frac{11}{3}$. In the standard model this simple prediction is modified by higher-order QCD effects due to the radiation of gluons, and by electroweak effects coming from annihilations via the Z^0 boson. The inclusion of these effects results in the production[3]

$$R=3\sum_q[\tfrac{1}{2}\beta_q(3-\beta_q^2)R_V^q(1+C_{\rm QCD}^V)+\beta_q^3R_{AA}^q(1+C_{\rm QCD}^A)]\ , \tag{1.1}$$

where

$$R_V^q=e_q^2-8e_qg_V^eg_V^q{\rm Re}(\chi)+16(g_V^{e2}+g_A^{e2})g_V^{q2}|\chi|^2\ ,$$

$$R_{AA}^q=16(g_V^{e2}+g_A^{e2})g_A^{q2}|\chi|^2\ ,$$

and

$$\chi=\frac{1}{16\sin^2\theta_W\cos^2\theta_W}\frac{s}{s-M_Z^2+iM_Z\Gamma_Z}\ .$$

Here q is an index running over the quark flavors and β_q is the corresponding quarks's velocity in the center-of-mass system. The quantities g_A^q and g_V^q are the quark axial-vector and vector coupling constants, which are specified by the model to the $g_A^q=\frac{1}{2}$ $(-\frac{1}{2})$ and $g_V^q=\frac{1}{2}-\frac{4}{3}\sin^2\theta_W$ $(-\frac{1}{2}+\frac{2}{3}\sin^2\theta_W)$ for the quark charge, $e_q=+\frac{2}{3}e$ $(-\frac{1}{3}e)$, where θ_W is the Weinberg angle. The electron axial-vector and vector constants g_A^e and g_V^e are specified by the model to be $g_A^e=-\frac{1}{2}$ and $g_V^e=-\frac{1}{2}+2\sin^2\theta_W$. The QCD terms $C_{\rm QCD}^V$ and $C_{\rm QCD}^A$ depend only on the scale parameter $\Lambda_{\overline{\rm MS}}$ ($\overline{\rm MS}$ denotes the modified minimal-subtraction scheme); third-order expressions for these factors are given in the Appendix. Thus, the standard-model relation for R depends only on $\sin^2\theta_W$, M_Z, and $\Lambda_{\overline{\rm MS}}$, which have been experimentally determined to be $\sin^2\theta_W=0.230\pm0.0048$,[4] $M_Z=91.09\pm0.06$ GeV/c^2,[5] and $\Lambda_{\overline{\rm MS}}=0.13^{+0.11}_{-0.06}$ GeV (for $N_F=5$).[6] R is insensitive to the value of Γ_Z the total decay width of the Z^0, at center-of-mass energies considered in this paper; we take it to be 2.5 GeV/c^2, which agrees with the recent measurements.[5]

Our previously reported values of R for $\sqrt{s}$ from 56 to 57 GeV are somewhat higher than the standard-model predictions;[2] similar results were reported by the other TRISTAN groups.[7,8] In the framework of the model, these results are most easily accommodated by taking the Z^0 mass to be $M_Z=88.6^{+2.0}_{-1.8}$ GeV/c^2, somewhat lower than the combined value from the two direct production measurements of the UA1[9] and UA2[10] experiments at the CERN $p\bar{p}$ collider, $M_Z=91.9\pm1.8$ GeV/c^2. The recent precise determinations of $M_Z=91.09\pm0.06$ GeV/c^2 virtually remove any ambiguity from the theoretical values for R and eliminates a lower value of M_Z as a cause of higher R values at TRISTAN energies.[5] Varying the values of the parameters within their quoted error changes the calculated values of R over the TRISTAN energy region by 1.2%, much smaller than typical experimental errors.

II. THE AMY DETECTOR

The AMY detector located at the OHO experimental hall of the TRISTAN e^+e^- storage ring, is a general-purpose detector based on a 3-T superconducting solenoidal magnet that is coaxial to the e^+e^- beam line with an inner radius of 1.2 m. Charged particles and γ rays are detected by cylindrical tracking chambers and electromagnetic shower calorimeters located inside of the magnet. Drift chambers and scintillation counters located outside of the iron flux-return yoke of the magnet are used to identify muons. A schematic view of the detector is shown in Fig. 2. In this section we give brief descriptions of the various detector components.

A. The charged-particle tracking system

Charged particles exiting the TRISTAN vacuum at the AMY interaction region pass through an aluminum beam pipe of radius 11.5 cm and wall thickness 1.5 mm (which corresponds to 1.7% of a radiation length at normal incidence). Surrounding the beam pipe are two devices for measuring charged-particle trajectories: the inner tracking chamber (ITC) and the central drift chamber (CDC).

The ITC[11] consists of four layers of drift tubes (aluminized plastic tubes with 16-μm-diam anode wires stretched along their axes) ranging in diameter from 5.5 to 6 mm. Each layer provides a position measurement of trajectory coordinates in the plane perpendicular to the beam direction (the r-ϕ plane) with a spatial resolution of $\sigma\sim80$ μm. The gas in the ITC (50% Ar, 50% C_2H_6) is pressurized

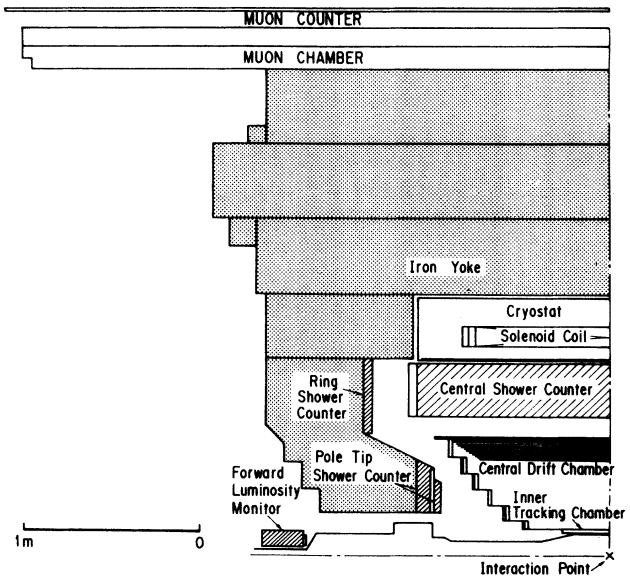

FIG. 2. A schematic view of the AMY detector.

to 1.46 atmospheres to improve the spatial resolution. The ITC extends from a radius of 12.2 to 14.2 cm and its fiducial length along the beam direction (the z axis) is 55 cm.

The CDC, located just outside the ITC, has 40 cylinders of wire drift cells extending out to a radius of 65 cm. Twenty-five of the cylinders, consisting of 5616 individual drift cells each approximately 6 mm in diameter, have wires parallel to the z axis for measuring the r-ϕ coordinates of trajectory points; the other 15 cylinders, consisting of 3432 cells, have wires at a small angle (typically 5°) relative to the beam direction to provide small-angle stereo measurements of z coordinates. For most of the results being reported here, the CDC was filled with a gas mixture (Ar 89%, CO_2 10%, CH_4 1%) at atmospheric pressure. All of the $\sqrt{s}=54$- and 61.4-GeV data and a portion of the $\sqrt{s}=60$- and 60.8-GeV data were taken with a 50:50 mixture of neon and ethane.

The cylinders are arranged in six superlayers of increasing length. Each superlayer provides a local determination of the track vector (position and direction), which enables quick estimates of multiplicity and momenta of the charged particles for triggering the data-acquisition system and facilitates the recognition of tracks in the off-line analysis. The hexagonal shape of the cells results in staggered cells which simplifies the resolution of the left-right ambiguities. The almost circular cell shape is instrumental in achieving a good spatial resolution in the presence of the 3-T magnetic field, where the Lorentz angle of the drifting electrons can be as large as 80°.

The average spatial resolution of the axial (stereo) cells of the CDC is $\sigma\sim 125$ (195) μm. The overall resolution of the central tracking devices (ITC and CDC) is estimated from Bhabha-scattering events ($e^+e^-\rightarrow e^+e^-$) to be $\Delta p_t/p_t \simeq 0.6\% \times [p_t\ (\mathrm{GeV}/c)]$ for high-momentum tracks with $|\cos\theta|<0.87$. The CDC and the techniques used to calibrate it are described in detail in Ref. 12, and the track-finding algorithms are explained in Ref. 13.

B. The electromagnetic shower counter

The barrel electromagnetic shower counter[14] (SHC) is a cylindrical ring comprised of six sextants. Each sextant subtends an angle of 60° in ϕ, and occupies the region from 80 cm $\leq r \leq$ 110 cm and $|\cos\theta| \leq 0.75$. Each sextant consists of an alternation of 20 layers or proportional tubes and 19 layers of lead, totaling $14.5/|\sin\theta|$ radiation lengths. The detector is operated with a gas mixture of 49.3% argon, 49.3% C_2H_6, and 1.4% alcohol at a voltage of 2150 V.

The individual cells are extruded resistive plastic tubes 222 cm in length with a 50-μm anode wire stretched through the center of each tube. Facing the outer surfaces of each tube layer are double-sided printed circuit boards with rectangular cathode strips that are sensitive to induced signals from the anode wires. The boards provide segmentation in 14-mrad intervals in the θ and ϕ directions. The signals are joined into groups within the detector. In the case of the θ and ϕ signals, strip signals are combined in a tower arrangement into subgroups providing five measurements of the longitudinal shower development. In the case of the anode wires, signals from about ten adjacent tubes in a given layer are tied together. This arrangement results in a total of about 11 000 cathode and 960 anode channels.

Each sextant is a self-contained gas-tight unit with four monitor tubes containing radioactive ^{55}Fe sources located inside. These tubes measure gain variations caused by changes in gas composition, atmospheric pressure, and temperature.

Tests performed with prototype units and with actual sextants placed into a 1–5-GeV test beam indicated spatial resolutions for minimum ionizing particles of $\sigma=4$ mm, which translates into an angular resolution in AMY of $\sigma_{\theta,\phi}=5$ mrad. The energy resolution determined in the test beam agreed with expectations, based on the EGS4 Monte Carlo program[15] of $\Delta E/E=0.25/\sqrt{E\ (\mathrm{GeV})}$ with no magnetic field. We study the detector's performance in the 3-T field of the AMY detector using electrons from Bhabha events and from the two-photon process $e^+e^-\rightarrow e^+e^-e^+e^-$. The energy resolution is found to be degraded to $\Delta E/E=0.23/\sqrt{E\ (\mathrm{GeV})}+0.06$.

C. The superconducting magnet

The 3-T magnetic field is produced by an eight-layer coil made of a Nb/Ti superconducting cable that contains both Cu and Al for stabilization. The coil is embedded in a hexagonal iron return yoke.[16] Because all of the detection devices, with the exception of the muon identification system, are inside the coil, no special efforts were made to minimize the coil thickness and a conventional pool-boiling cooling method is used. A 500-A electric current provides the 3-T field; the stored energy is 40 MJ.

We measured the magnetic field along the beam line with all the detector components in place and compared

the result with a calculation done using the computer program POISSON.[17] The agreement was within ±03.% after a proper normalization of the central field. The field strength elsewhere inside the detector is then estimated by POISSON, which is expected to give an error of less than 0.4% inside the tracking devices. There is sizable nonuniformity in the field strength; over the tracking volume of the CDC, the field strength varies from −18% to +5% of its value at the interaction point.

D. The muon-identification system

The material of the SHC, the magnet coil, and the iron return yoke amounts to 1.3 kg/cm^2 (the equivalent of 1.6 m of iron) at normal incidence, which corresponds to about nine absorption lengths for strongly interacting particles. Particles penetrating this material are identified by the muon-detection system (MUO), consisting of four layers of drift cells and one layer of plastic scintillator, situated outside of the iron return yoke and covering the angular region $|\cos\theta| < 0.74$. The cells have a 5 cm × 10 cm cross section and a spatial resolution that is typically 1 mm. Two layers of cells are 6.5 m long and have wires parallel to the beam axis; two layers of cells range in length from 2.8 to 4.1 m and have wires perpendicular to the beam. The combined system has a track-segment reconstruction efficiency greater than 98%. Scintillation counters, located just outside the drift chambers, measure the time of penetrating particles relative to the beam-crossing time with a precision of about 3 ns, providing discrimination against backgrounds from cosmic rays which are randomly distributed in time.

E. The end-gap detectors

Particles emitted at smaller angles are detected in the pole-tip counter (PTC), which covers the region $0.90 < \cos\theta < 0.97$ and the ring shower counter (RSC), covering $0.78 < \cos\theta < 0.90$.

The PTC[18] consists of two modules of lead-scintillator calorimeters with a plane of proportional tubes between them. The total thickness of calorimeter modules is 14 radiation lengths. This device provides measurements of the energies and positions of electrons and photons and the positions of other charged particles incident on it. Its primary function is the determination of the luminosity by detecting Bhabha-scattering events. Its energy resolution is $\Delta E/E = 29\%/\sqrt{E\ (\mathrm{GeV})} + 6\%$. The position resolution is about 4 and 14 mrad for the θ and ϕ directions, respectively.

The RSC consists of two layers of lead and scintillator (1-cm-thick lead and 1-cm-thick scintillator for each layer) and signals the presence of showering particles (either electrons or photons). Charged tracks that enter the RSC are visible in minimum of 15 CDC layers and electrons among these tracks can be identified by comparing the RSC measured energy with the CDC measured momentum. The RSC energy resolution is $\Delta E/E = \sqrt{29^2 + 39^2/E\ (\mathrm{GeV})}\%$.

In addition, there are counters in the forward region ($\theta \sim 4.0°$) that are used to measure the instantaneous luminosity and to monitor beam-related background radiation levels.

F. Triggering

The frequency of beam crossings at TRISTAN is 200 kHz, and the capacity of the AMY data-acquisition system is ~3 Hz. In the internal between beam crossings, a decision is made as to whether or not an event of possible interest has occurred. In order to be sensitive to as many e^+e^- processes as possible, the trigger requirements for the detector are kept as loose as possible, consistent with the maximum possible 3 Hz. As a result we typically accumulate approximately 5000 events/h, of which only one or two are actual annihilation to multihadrons.

Bhabha events in the PTC, from which we determine the integrated luminosity, generate triggers in two ways. The first is a coincidence of two sections of the counter (front and rear) on the same side of the interaction region. The second is a coincidence of the rear sections of the counter on both sides of the interaction region. Together these triggers are perfectly efficient for Bhabha events within the PTC fiducial cuts. Large-angle Bhabha events generate triggers as a result of total energy deposition in the SHC and, independently, as a result of radial track segments detected in the ITC and the superlayers of the CDC.

For multihadron events, triggers are generated via three quasi-independent systems. The simplest of these requires that an analog sum of the pulse heights from the 48 SHC anode towers exceed a threshold. The threshold, which is typically ~3 GeV, is adjusted to produce a trigger rate not exceeding ~0.3 Hz. The second system requires the presence of four or more radial track segments in each of the outer five CDC superlayers. The third system places a weak demand on the presence of CDC track segments but also requires detection of two or more track segments in the ITC. All three systems render a decision in less than 2.0 μs, and the combined rate is much less than the 3.0-Hz capacity of the data-logging system. More than 95% of the events in the hadronic sample satisfied the requirements of all three trigger systems.

G. Data acquisition

A computer-controlled FASTBUS system digitizes analog signals from the SHC, PTC, RSC, and ITC and timing signals from the CDC, ITC, and MUO for each event. Triggers and high-voltage status are recorded for each event by a CAMAC system. Environmental conditions and the SHC monitor tube gain are measured periodically. All the digitized data are read in by a Vax 11/780 computer, where they are temporarily stored. Here, various checks are made to monitor operation of the entire detection system. The data are then sent via an optical link to a FACOM M780 computer, where the data format is immediately rearranged for the convenience of later analyses. The data are stored in a cassette-type library from which it is subsequently accessed for off-line analyses.

H. Track definitions

In the event reconstruction, charged tracks are required to have at least eight axial and five stereo hits that fit to a helix, be emitted in the angular range of $|\cos\theta| \leq 0.85$, and originate from points within $r \leq 5$ cm and $|z| \leq 15$ cm of the interaction point. Energy clusters in the SHC that are greater than 0.2 GeV are interpreted as showers. In the data samples taken at 54 and 58.5 GeV and above, only showers with $|\cos\theta| \leq 0.73$ are accepted. At other beam energies, which were presented previously,[1,2] this angle cut is not required. Any shower with energy less than 1 GeV and within 3 cm of the extrapolated position of a charged track was associated with that track and not treated as an independent particle.

III. DETERMINATION OF R

The R ratio is determined from the relation

$$R = \frac{N_{\rm ev} - N_{\rm bkg}}{\epsilon(1+\delta)\int L\,dt\,\sigma_{\mu\mu}(s)}\ , \tag{3.1}$$

where $N_{\rm ev}$ is the number of observed multihadron annihilation events, $N_{\rm bkg}$ is the estimated number of background events remaining in the sample, ϵ is the detection efficiency for hadronic events, $1+\delta$ is a correction factor for radiative effects, $\int L\,dt$ is the integrated luminosity, and $\sigma_{\mu\mu}(s)$ $(=4\pi\alpha^2/3s)$ is the lowest-order QED cross section for $e^+e^- \rightarrow \mu^+\mu^-$ at the same center-of-mass energy.

A. Event selection

Multihadron annihilation events are selected by requiring five or more charged tracks, a total visible energy[19] ($E_{\rm vis}$) greater than half of the center-of-mass energy, a momentum imbalance along the beam direction[20] of magnitude less than $0.4E_{\rm vis}$, and more than 3 (5) GeV of energy deposited in the SHC at center-of-mass energies of 50 and 52 (54–61.4) GeV.

Computer-generated event displays of the 3843 events that pass these selection criteria were scanned by physicists. As a result of this scan, 22 events that were caused by complicated cosmic-ray showers, 27 events due to beam-wall interactions, and 12 multiply radiative Bhabha events were eliminated. These events are easily recognizable in the event display; two independent scans by physicists rejected the same events.

B. Efficiency

The detection efficiency for multihadron annihilation events is the product of the detector acceptance and the efficiencies of the event-selection criteria, the triggers, and the data-acquisition system.

The acceptance of the detector and the efficiency of the event-selection criteria for multihadron annihilation events were determined by means of a Monte Carlo simulation. Hadronic events were generated with the LUND 63 parton-shower (PS) program,[21] which includes initial-state radiation using methods developed by Berends, Kleiss, and Jadach[22] (BKJ). The PS program generates showers of quarks and gluons in a cascade process where each parton branches into two partons ($q \rightarrow qg$, $g \rightarrow gg$, $g \rightarrow q\bar{q}$) using branching probabilities calculated in the leading-logarithmic approximation of QCD, as given by the Altarelli-Parisi equations.[23] This cascade proceeds until the parton virtual mass reaches a cutoff value (taken to be 1 GeV/c^2), at which stage hadrons are formed by means of the string-fragmentation (SF) model.[24] In the SF model, hadrons are produced from partons via the breaking of color flux tubes that are stretched between opposite color charges. Studies of the charged multiplicity, global event shapes, inclusive charged-particle spectra, and particle-flow distributions for the same events used for the results reported here show quite good agreement with the predictions of the LUND PS program.[25,26] The original BKJ calculation includes initial-state radiation, vertex corrections for both γ and Z^0 propagators, QED vacuum-polarization terms, and final-state radiation, but does not include all box diagrams, nor the full electroweak vertex corrections and vacuum-polarization terms. Corrections for final-state radiation are not included in the BKJ calculation that is implemented in the PS event generator. All of the above are included in the program of Fujimoto and Shimizu[27] (FS), which we use to calculate $1+\delta$ (see below). We estimate that differences in ϵ computed using BKJ instead of FS are negligible.

Events produced by the generator are passed through a series of Monte Carlo computer programs that simulate the response of the AMY detector. Electromagnetic showers initiated by photons and electrons are modeled with the EGS4 program;[15] hadron showers are modeled by the GRANT program.[28] The drift-chamber response is smeared with a resolution function determined by matching to the observed data. The response of the detector elements is converted into a form identical to the actual data records. Simulated data and real data are subjected to the same analysis programs. We determine ϵ from the fraction of simulated PS events that pass our event-selection criteria. Approximately 2000 Monte Carlo–simulated multihadron events were scanned by physicists using the same acceptance criteria used for the actual data sample. None of the simulated events were rejected.

The detection efficiency is also affected by failures in data recording. For example, poor running conditions of the storage ring occasionally caused high-voltage trips that disabled the CDC for short periods of time without interrupting the luminosity measurement in the PTC. We have determined the number of Bhabha events in the SHC that have no corresponding CDC tracks because of these failures and also the number of Bhabha events in the PTC that occurred while the high voltage was off in more than 15 layers of the CDC. From these tallies we estimate that ϵ should be decreased by 0.0–0.9% for data with center-of-mass energies other than 54 GeV and 5% for the 54-GeV data, which was taken under particularly poor beam conditions. The trigger efficiency is estimated by comparing the response of different, redundant, triggering systems. Since this is estimated to be

better than 99.7%, no correction for trigger efficiency is applied to ϵ.

C. Background estimates

From the z-vertex distribution obtained with the cut on $|z|$ relaxed, we deduce the contamination from beam-gas collisions to be less than 0.3%. More Carlo simulations of multihadron events originating from $e^+e^-\to\tau^+\tau^-$ and two-photon processes ($e^+e^-\to e^+e^-+$hadrons)[29,30] indicate center-of-mass energy-dependent contaminations of 0.7–1.1% and 0.5–0.7%, respectively. For two-photon reactions, we consider three processes: hadronic (vector-mass-dominance model),[31] $\gamma\gamma\to 2$ jets (quark-parton model),[31] and $\gamma\gamma\to 3$ jets.[32] These give individual contaminations of 0.12–0.15%, 0.23–0.45%, and 0.11–0.13%, respectively.

D. Radiative corrections

We calculate $1+\delta$ using the FS radiative-correction program that includes full electroweak effects up to $O(\alpha^3)$.[28] The radiative corrections are a function of the t-quark mass m_t, the Z^0 mass M_Z, the $W^\pm$ mass M_W, and the Higgs-boson mass M_H. In fact, if M_W is not fixed but taken as its standard-model value $M_W=M_Z f(G_F,\alpha,m_t,M_H)$, the results are rather insensitive to the assumed values for the masses m_t and M_H. The biggest uncertainty comes from the unknown mass of the t quark; changing it from 45 to 200 GeV/c^2 increases by $1+\delta$ by 0.2% at $\sqrt{s}=50$ GeV, and decreases it by 0.5% and 1.3% at $\sqrt{s}=56$ and 60 GeV, respectively. In the previous analysis[2] we used $m_t=45$ GeV/c^2, $M_Z=92$ GeV/c^2, and $M_H=100$ GeV/c^2; here we use $m_t=150$ GeV/c^2, $M_Z=91.1$ GeV/c^2, and $M_H=100$ GeV/c^2. The present values of $1+\delta$ are lower than the previous ones by 0.0%, 0.4%, and 1.0% at $\sqrt{s}=50$, 56, and 60 GeV, respectively. Here the different values of m_t are primarily responsible for this change of $1+\delta$; the effects of different values of M_Z on $1+\delta$ are less than 0.3%. The values we use for $1+\delta$ are higher than those calculated with the BKJ program. The differences are 1.6, 2.3, and 3.3% with $\sqrt{s}=50$, 56, and 60 GeV, respectively.[33] The effects of weak-boson propagators on the vertex corrections and final-state radiation are primarily responsible for this discrepancy.

E. Luminosity determination

We infer the e^+e^- luminosity from the number of Bhabha-scattering events detected in the PTC. Bhabha events are selected by requiring two showering particles, each with energy greater than 8 GeV, with a back-to-back collinearity angle that is less than 10°. For Bhabha events observed in the PTC, where we do not have charged-particle tracking information, we make corrections for a 1.4% and 2.5% contamination from $e^+e^-\to\gamma\gamma$ and $e^+e^-\to e^+e^-\gamma$ events, respectively, which are determined from an order-α^3 QED calculation.[34,35,36] For Bhabha events detected in the SHC we require that charged tracks in the CDC match to the SHC showers. The integrated luminosity for each energy, as determined from the number of Bhabha events observed in the PTC, is listed in Table I. In this table we list the point-to-point errors. Independent determinations of the integrated luminosity, using Bhabha events in the SHC, give results that are consistent with the end-cap measurement. These measurements are also summarized in Table I, where only the statistical errors are listed. The ratio of the two measurements for all run periods combined is

$$\frac{(\int L\,dt)_{\rm PTC}}{(\int L\,dt)_{\rm SHC}}=0.993\pm0.011\ ,$$

where we considered only point-to-point systematic and statistical errors.

TABLE I. A summary of the integrated luminosities measured by two independent processes: Bhabha scattering in the PTC region (PTC Bhabha) and Bhabha scattering in the SHC region (SHC Bhabha). The point-to-point errors are listed for the PTC luminosities, while only the statistical errors are shown for the SHC luminosities. There is an additional overall normalization error of 1.8% for the PTC luminosities.

	Integrated luminosity	
	PTC Bhabha	SHC Bhabha
$\sqrt{s}$ (GeV)	$0.92<\lvert\cos\theta\rvert<0.96$ (pb^{-1})	$\lvert\cos\theta\rvert<0.73$ (pb^{-1})
50	0.636±0.016	0.64±0.04
52	3.976±0.080	3.88±0.10
54	0.531±0.017	0.43±0.04
55	3.266±0.039	3.42±0.10
56	5.933±0.053	6.06±0.13
56.5	0.994±0.022	1.05±0.06
57	4.398±0.046	4.44±0.12
58.5	0.801±0.016	0.73±0.05
59.0	0.721±0.020	0.63±0.05
59.05	0.504±0.013	0.46±0.04
60.0	3.551±0.044	3.59±0.11
60.8	3.481±0.064	3.73±0.12
61.4	4.287±0.060	4.17±0.12

F. Systematic errors

We now detail the sources of error in our determination of the R values. The energy-dependent systematic errors consist of the errors associated with the luminosity measurement, the calculations of $\epsilon(1+\delta)$, and the calculation of data-recording failures. The overall normalization uncertainty contains energy-independent systematic errors in the luminosity determination, the detection-efficiency estimation, radiative corrections, event selection, and the background subtraction, which, when added in quadrature, result in a total 3.2% normalization error. The errors are summarized in Table II. In the remainder of this section we discuss the entries in Table II. A more detailed discussion of the systematic errors is given in Ref. 13.

The systematic error of the luminosity measurements (1.8%) is dominated by the uncertainties in alignment

TABLE II. A summary of the systematic errors in the measurement of R values. For each item, energy-dependent point-to-point errors are given by 13 numbers corresponding to $\sqrt{s}=50$, 52, 54, 55, 56, 56.5, 57, 58.5, 59, 59,05, 60, 60.8, and 61.4 GeV while only one number is displayed for the case of energy-independent errors. See the text for details.

Systematic errors	(%)
Luminosity	
Statistics	2.5,1.1,3.2,1.2,0.9,2.2,1.1,2.0,2.8,2.6,1.2,1.5,1.2
Radiative correction, acceptance	1.3
Background	0.2
Correction for dead sections	0.0,1.7,0.8,0.0,0.0,0.0,0.0,0.0,0.0,0.0,0.0,0.0,1.1,0.6
Trigger efficiencies	0.2
Chamber efficiencies	0.1
Alignment	1.2
Detector acceptance	
Monte Carlo statistics	0.8,0.8,0.4,0.6,0.6,0.7,0.7,0.4,0.4,0.4,0.4,0.4,0.4
Monte Carlo scheme	0.7
Fragmentation	0.9
Detector simulation	0.5
Data-recording failure	$^{+0.94}_{-0.00}$,0.13,0.56,0.17,0.15,0.90,0.34,0.08,0.11,0.07,0.08,0.07,0.09
Event selection	
Selection cuts	1.5
Calibration/reconstruction	0.8
Background	
$\tau\tau$, two photon	0.3
Beam gas	0.3
Visual scan	0.2
Radiative corrections	
$k_{\max}$ dependence	1.0
Hadronic vacuum polarization	0.8
m_t, M_{H^0} dependence	0.8
Point-to-point error	2.8,2.2,3.4,1.4,1.1,2.5,1.3,2.0,2.8,2.6,1.3,1.9,1.4
Overall normalization error	3.2

(1.2%) and the effects of higher-order radiative corrections (1.3%). The error in luminosity due to uncertainty in alignment is reduced from the 3.0% value used in our previous analysis to 1.2% because of a refinement of our estimates of the position uncertainties of the PTC. The deviation of the PTC position from the nominal one in the r-ϕ plane is estimated by requiring collinearity for Bhabha events in the PTC, where run-by-run coordinates of the primary vertex point, determined from charged tracks, are used. The deviation is found to be less than 1 mm (compared to the estimated precision of 2 mm in the previous analysis) and is consistent with direct survey measurements of the detector positions. This translates into a 0.7% error in luminosity. The deviation of the PTC position in the z direction is estimated to be 2 mm (it was taken as 5 mm in the previous analysis) from survey data, which results in a 0.8% error in luminosity. Accordingly, the total error of luminosity measurements due to uncertainty in alignment is estimated to be 1.2%. A section of the PTC was not operational for some portions of the 52-, 54-, 60.8,- and 61.4-GeV data samples, resulting in additional systematic errors in the luminosity of 1.7%, 0.8%, 1.1%, and 0.6% at $\sqrt{s}=52$, 54, 60.8, and 61.4 GeV, respectively. These errors reflect the uncertainty in the position and gain of the nonoperating section.

The error in the detection efficiency is estimated from the range of its variation when calculated using different Monte Carlo event generators and different detector simulators. For event generators we use the LUND PS model,[21] the LUND 6.2 model,[37] and the EPOCS[29] $O(\alpha_s^2)$ matrix-element model. In the last two cases we use both the string-fragmentation and independent fragmentation schemes. We see changes in ϵ of 0.7% (0.9%) for the different parton production (fragmentation) schemes and 0.5% for ambiguities in the parameters used in the detector simulator, which we use as the estimate of the systematic error. Additional errors for the detector efficiency are point-to-point errors ranging from 0.07% to 0.9% due to failures in data acquisition.

From the variation in the number of selected events when changes are made in the selection criteria, SHC calibration constants, and reconstruction program, we estimate the systematic errors associated with the event-selection criteria and calibration reconstruction to be 1.5% and 0.8%, respectively, resulting in a total sys-

tematic error for the event selection of 1.7%. In Figs. 3(a) and 3(b) we show comparisons of the measured and simulated distributions for the visible energy and the longitudinal-momentum balance, respectively. The data presented in these figures are selected with all other cuts except for the visible energy or the momentum balance cut, respectively. The Monte Carlo distributions are normalized so that after the final cuts the number of simulated and measured events were the same. It is clear from the figures that the measured distributions for the quantities used for event selection are reproduced reasonably well by the Monte Carlo simulation.

The background subtraction uncertainty for τ pair production and two-photon processes is estimated to be 0.3%, which includes variation between different detector simulators and the effects of the uncertainty of the total

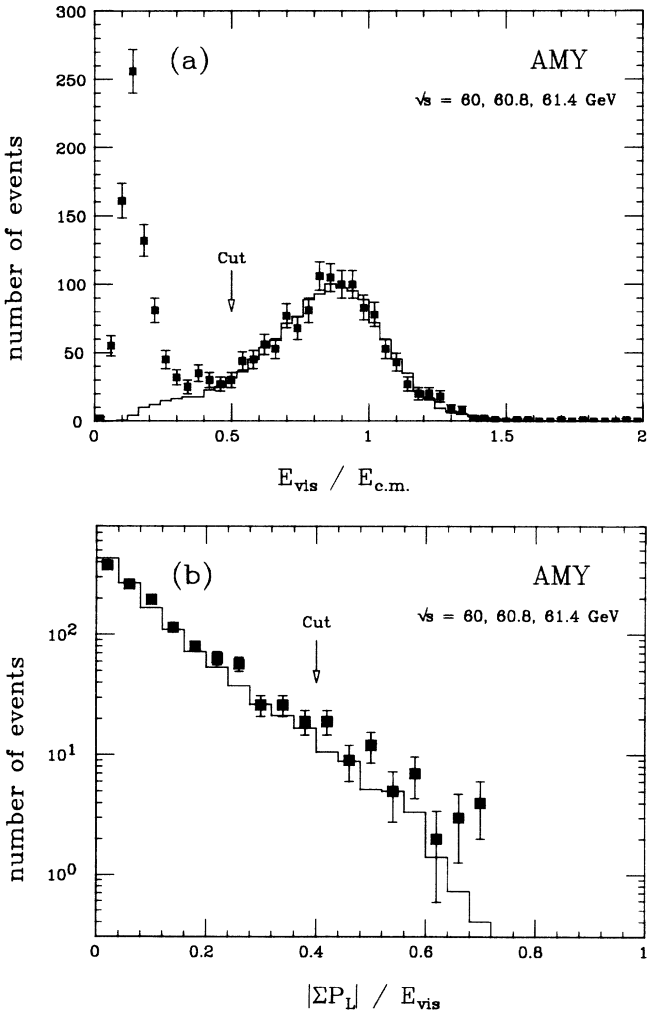

FIG. 3. (a) The visible-energy distribution. The data for $\sqrt{s} \geq 60$ GeV (points) are compared with the prediction of the LUND parton-shower model (histogram). The data are selected with all other cuts except for the visible energy cut and the position of the cut is indicated with an arrow. The Monte Carlo distribution is normalized so that after the final cut the number of simulated and measured events are the same. (b) A similar comparison for the longitudinal-momentum balance distribution.

cross section for $\gamma\gamma \rightarrow$hadrons. The subtraction error for beam-gas events that are detected upstream and downstream of the interaction point is dominated by the statistical uncertainty of 0.3%. The uncertainty in the background subtraction by visual scan is 0.2%, which corresponds to 10% of the number of rejected events. Adding these errors in quadrature results in the total 0.5% error associated with the background subtraction.

The radiative correction $1+\delta$ varies according to the maximum-allowed fractional energy of the radiated photon $k_{\max}$. This is nearly compensated by the variation in the detection efficiency ϵ resulting in a rather stable value for the product $\epsilon(1+\delta)$; the product varies by only 1.0% when $k_{\max}$ is changed from $0.99E_{\text{beam}}$ and $0.8E_{\text{beam}}$. Errors in the vacuum polarization component of $1+\delta$ arise from uncertainties in the total cross section for $e^+e^- \rightarrow$hadrons for $E_{\text{c.m.}} \leq 9$ GeV. If we change this cross section by 20%, the contribution from vacuum polarization varies by less than 0.8%, which we take as the systematic error. In the FS calculation we use a t-quark mass of 150 GeV/c^2; if we use $m_t = 80$ (200) GeV/c^2, the results change by less than +0.7% (−0.8%) over the center-of-mass energy range covered by this experiment. For the Higgs-boson mass we use 100 GeV/c^2; if we take it to be 15 (1000) GeV/c^2, the results change by a maximum of −0.2% (+0.4%), We include a 0.8% error due to the uncertainty of the t-quark and the Higgs-boson mass. (This error was not included in the previous analysis.[2]) Adding all the above in quadrature results in a total systematic error associated with the radiative corrections of 1.5%.

G. Results

The R-measurement results are summarized in Table III. In addition to the listed errors, which include only the point-to-point uncertainties, there is an overall normalization error of 3.2%. The R values for the 50–57-GeV data (except for that for 54 GeV) are slightly different from the previously reported results,[2] reflecting different assumptions for the t-quark mass and M_Z values used in the evaluation of the radiative corrections. The normalization error of 3.2% is somewhat smaller than the previously reported value of 4.1% due to the reevaluation of the systematic error in the luminosity measurement as described above.

IV. DISCUSSION

The R measurements are shown in Fig. 4, together with published results from the VENUS and TOPAZ experiments at TRISTAN as well as with lower-energy results from PEP, PETRA, CESR, and DORIS.[7,8,38–40] Here the R values for PEP and PETRA are taken from Ref. 38, which gives the R values for these experiments calculated with the same radiative-correction program of BKJ including Z^0 exchange, but excluding the effects of final-state radiation. We have adjusted the published R values from VENUS and TOPAZ for the effects of the extra diagrams and the different parametrizations of the radiative correction. (At PETRA and PEP energies these

TABLE III. A summary of R values. For the notation, see Sec. III of the text. Here R_{theory} is the prediction of the five-quark standard model with $M_Z=91.1$ GeV/c^2, $\sin^2\theta_W=0.230$, and $\Lambda_{\overline{\text{MS}}}=0.13$ GeV. Overall normalization error of R is 3.2%.

$\sqrt{s}$ (GeV)	N_{ev}	N_{bkg} $\tau\tau$	N_{bkg} 2γ	$1+\delta$	ϵ	$\epsilon(1+\delta)$	$\sigma_{\mu\mu}$ (pb)	R	R_{theory}
50	88	0.9±0.1	0.5±0.1	1.336	0.652	0.871	34.7	4.50±0.50	4.23
52	482	5.4±0.7	3.1±0.7	1.329	0.650	0.864	32.1	4.29±0.22	4.34
54	61	0.7±0.05	0.3±0.02	1.320	0.608	0.802	29.8	4.73±0.64	4.48
55	368	3.7±0.5	2.5±0.6	1.314	0.633	0.832	28.7	4.64±0.25	4.57
56	727	6.8±0.9	4.6±1.1	1.307	0.632	0.826	27.7	5.22±0.20	4.67
56.5	123	0.7±0.1	0.8±0.2	1.304	0.645	0.841	27.2	5.34±0.51	4.72
57	492	3.2±0.5	3.4±0.7	1.300	0.645	0.839	26.7	4.92±0.23	4.78
58.5	89	0.8±0.06	0.4±0.03	1.288	0.629	0.810	25.4	5.33±0.58	4.97
59	80	0.7±0.06	0.4±0.03	1.284	0.628	0.807	25.0	5.44±0.63	5.04
59.05	68	0.5±0.04	0.3±0.02	1.283	0.630	0.808	24.9	6.62±0.83	5.05
60	405	3.6±0.3	1.8±0.1	1.274	0.626	0.797	24.1	5.85±0.30	5.20
60.8	368	3.5±0.3	1.8±0.1	1.266	0.627	0.794	23.5	5.59±0.31	5.35
61.4	431	4.4±0.4	2.2±0.2	1.260	0.624	0.786	23.0	5.46±0.28	5.47

effects are negligible and we have not adjusted those data points.) The error bars in the figure represent total statistical and systematic errors added in quadrature. In Fig. 4 the solid curve indicates the prediction of the five-quark standard model with $M_Z=91.1$ GeV/c^2, $\sin^2\theta_W=0.230$, and $\Lambda_{\overline{\text{MS}}}=0.13$ GeV.

The standard-model curve lies consistently below the data points for center-of-mass energies above 11 GeV. The situation is somewhat improved if we treat $\Lambda_{\overline{\text{MS}}}$ as a free parameter and fit the SM curve to all of the data shown in Fig. 4 using the technique described in Ref. 38. In that case we find a value of $\Lambda_{\overline{\text{MS}}}=0.25^{+0.15}_{-0.12}$ GeV; the results are indicated as dot-dashed curves in Fig. 4. This change in $\Lambda_{\overline{\text{MS}}}$ has a small ($\simeq 0.6\%$) effect on the predicted values for R in the TRISTAN energy range. Fitting $\Lambda_{\overline{\text{MS}}}$ to only the data above $\sqrt{s}=11$ GeV yields the substantially higher value of $\Lambda_{\overline{\text{MS}}}=0.38^{+0.24}_{-0.18}$ GeV, and the predicted R values in the TRISTAN energy range are increased from the nominal ($\Lambda_{\overline{\text{MS}}}=0.13$ GeV) case by 1.0%. This higher value for $\Lambda_{\overline{\text{MS}}}$ fits the PEP and PETRA data well but still lies below our data points. We fit our data to the SM prediction (using $\Lambda_{\overline{\text{MS}}}=0.13$ GeV) by allowing for an overall normalization factor A and minimizing

$$\chi^2=\left[\frac{A-1}{\sigma^{\text{norm}}}\right]^2+\sum_i\left[\frac{R_i^{\text{meas}}-R^{\text{SM}}(s_i)}{\sigma_i^{p\text{-}p}}\right]^2,$$

where σ^{norm} is the overall normalization error, $\sigma_i^{p\text{-}p}$ is the point-to-point error of the ith measured point, and $R^{\text{SM}}(s_i)$ is the standard-model prediction of the value of R at the energy of the ith measured point. The results of the fit are $A=0.951$ and $\chi^2=14.5/(12\ \text{DF})$. In Fig. 5 we

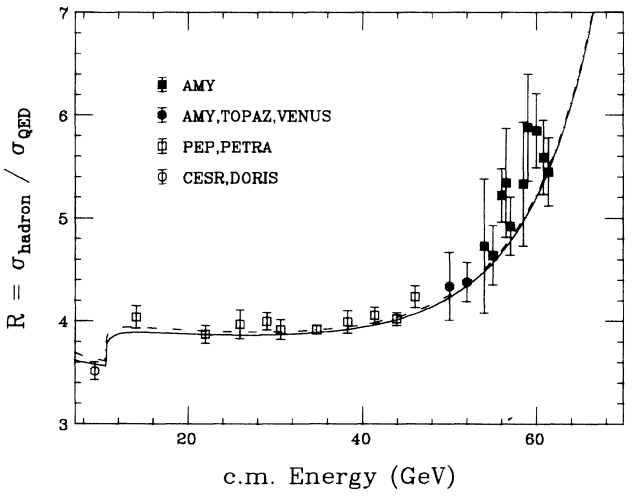

FIG. 4. Results of the measurements of R (solid squares) together with previously reported results at lower energies. The error bars include statistical and systematic errors. The data from the experiments at c.m. energies up to 52 GeV and the data at 59 and 59.05 GeV are combined for display purposes. The solid curve is the standard-model prediction for $\sin^2\theta_W=0.230$, $M_Z=91.1$ GeV/c^2, and $\Lambda_{\overline{\text{MS}}}=0.13$ GeV; the dot-dashed curve uses our fitted value of $\Lambda_{\overline{\text{MS}}}=0.25$ GeV.

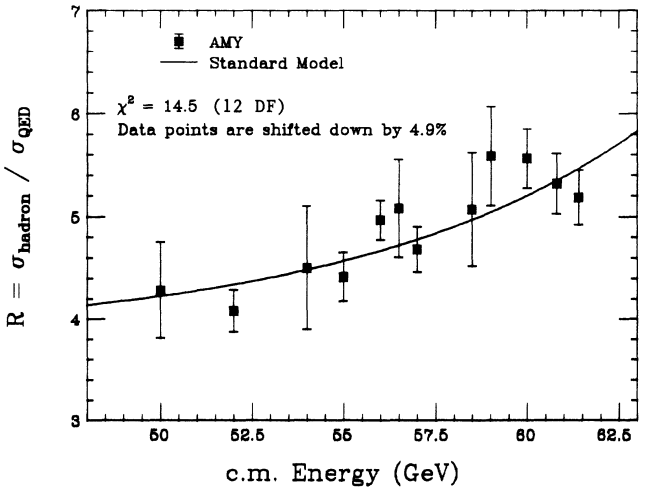

FIG. 5. The AMY results for R shifted down by 4.9% and compared with the standard-model prediction. The data at 59 and 59.05 GeV are combined for display purposes.

plot the measured values of R scaled by this result for A and superpose the standard-model curve.

V. CONCLUSION

The ratio R of the total cross section for e^+e^- annihilation into hadrons to the lowest-order QED cross section for $e^+e^-\to\mu^+\mu^-$ has been measured for center-of-mass energies ranging from 50 to 61.4 GeV. If we allow for an overall shift of -4.9%, about 1.5 times our estimated normalization error, the results are consistent with the standard-model predictions.

ACKNOWLEDGMENTS

We thank the TRISTAN staff for the excellent operations of the storage ring. In addition we acknowledge the strong support provided by the staffs of our home institutions. We thank W. Bartel for carefully reading the manuscript. This work has been supported by the Japan Ministry of Education, Science, and Culture (Monbusho) and Society for the Promotion of Science, the U.S. Department of Energy, and the National Science Foundation, the Korea Science and Engineering Foundation and Ministry of Education, and the Academia Sinica of the People's Republic of China.

APPENDIX: THE QCD CORRECTION TERMS $C^V_{\rm QCD}$ AND $C^A_{\rm QCD}$

Th QCD terms in Eq. (1.1), $C^V_{\rm QCD}$ and $C^A_{\rm QCD}$ have recently been calculated up to the third order in the QCD coupling strength α_s using the modified minimum-subtraction ($\overline{\rm MS}$) scheme:[41]

$$C^{V(A)}_{\rm QCD}=C_1^{V(A)}\left[\frac{\alpha_s}{\pi}\right]+C_2^{V(A)}\left[\frac{\alpha_s}{\pi}\right]^2+C_3^{V(a)}\left[\frac{\alpha_s}{\pi}\right]^3,$$

where

$$C_1^V=\frac{4\pi}{3}\left[\frac{\pi}{2\beta_q}-\frac{3+\beta_q}{4}\left[\frac{\pi}{2}-\frac{3}{4\pi}\right]\right],$$

$$C_1^A=\frac{4\pi}{3}\left[\frac{\pi}{2\beta_q}-(\tfrac{19}{10}-\tfrac{22}{5}\beta_q+\tfrac{7}{2}\beta_q^2)\left[\frac{\pi}{2}-\frac{3}{4\pi}\right]\right],$$

$$C_2^{V(A)}=1.986-0.115N_f,$$

and

$$C_3^{V(A)}=70.985-1.2N_f-0.005N_f^2-1.679\frac{\left[\sum e_q\right]^2}{\left[3\sum e_q^2\right]}.$$

Here N_f is the number of quark flavors and $a\ (=\alpha_s/\pi)$ is related to $\Lambda_{\overline{\rm MS}}$, the QCD scale parameter, by

$$\beta_0\ln\frac{s}{\Lambda^2_{\overline{\rm MS}}}=\frac{1}{a}-c_1\ln\frac{c_1}{\beta_0}+c_1\ln\frac{c_1a}{1+c_1a}+\frac{c_1}{2}\ln\frac{(1+c_1a)^2}{1+c_1a+c_2a^2}+\frac{2c_2-c_1^2}{\sqrt{\Delta}}\left[\arctan\left[\frac{c_1+2c_2a}{\sqrt{\Delta}}\right]-\arctan\left[\frac{c_1}{\sqrt{\Delta}}\right]\right],$$

where

$$c_1=\frac{\beta_1}{\beta_0},\quad c_2=\frac{\beta_2}{\beta_0},\quad \Delta=4c_2-c_1^2,$$

$$\beta_0=\tfrac{1}{12}(33-2N_f),\quad \beta_1=\tfrac{1}{48}(306-38N_f),$$

and

$$\beta_2=\tfrac{1}{64}(\tfrac{2857}{2}-\tfrac{5033}{18}N_f+\tfrac{325}{54}N_f^2).$$

[1]AMY Collaboration, H. Sagawa *et al.*, Phys. Rev. Lett. **60**, 93 (1988).

[2]AMY Collaboration, T. Mori *et al.*, Phys. Lett. **48B**, 499 (1989).

[3]T. Appelquist and H. D. Politzer, Phys. Rev. D **12**, 1404 (1975); M. Dine and J. Sapirstein, Phys. Rev. Lett. **43**, 668 (1979); K. G. Chetyrkin *et al.*, Phys. Lett. **85B**, 277 (1979); W. Celmaster and R. J. Gonsalves, Phys. Rev. Lett. **44**, 560 (1980); J. Jersak, E. Laermann, and P. M. Zerwas, Phys. Rev. D **25**, 1218 (1982); W. J. Marciano, *ibid.* **29**, 580 (1984); S. Gusken *et al.*, Phys. Lett. **155B**, 277 (1985).

[4]U. Almaldi *et al.*, Phys. Rev. D **36**, 1385 (1987).

[5]Mark II Collaboration, G. Abrams *et al.*, Phys. Rev. Lett. **63**, 724 (1989); CDF Collaboration, F. Abe *et al.*, *ibid.* **63**, 720 (1989); L3 Collaboration, B. Adeva *et al.*, Phys. Lett. B **231**, 509 (1989); ALEPH Collaboration, D. Decamp *et al.*, *ibid.* **231**, 519 (1989); OPAL Collaboration, M. Z. Akrawy *et al.*, *ibid.* **231**, 530 (1989); DELPHI Collaboration, P. Aarnio *et al.*, *ibid.* **231**, 539 (1989).

[6]We have taken the value of 200^{+150}_{-90} MeV for $\Lambda_{\overline{\rm MS}}$ in the case of $N_f=4$ from Particle Data Group, Phys. Lett. B **204**, 100 (1988), and converted it into the value for $N_f=5$.

[7]VENUS Collaboration, H. Yoshida *et al.*, Phys. Lett. B **198**, 570 (1987); VENUS Collaboration, Y. Unno *et al.*, in *Proceedings of the XXIV International Conference on High Energy Physics*, Munich, West Germany, 1988, edited by R. Kotthaus and J. H. Kühn (Springer, Berlin, 1989).

[8]TOPAZ Collaboration, I. Adachi *et al.*, Phys. Rev. Lett. **60**, 97 (1988); TOPAZ Collaboration, M. Yamauchi *et al.*, in *Proceedings of the XXIV International Conference on High Energy Physics* (Ref. 7).

[9]UA1 Collaboration, G. Arnison *et al.*, Phys. Lett. **166B**, 484 (1986).

[10]UA2 Collaboration, R. Ansari *et al.*, Phys. Lett. B **186**, 440 (1987).

[11]M. Frautschi *et al.* (unpublished).

[12]K. Ueno *et al.* (unpublished).

[13]T. Mori, Ph.D. thesis, University of Rochester Report No. UR-1104, 1988.

[14]A. Abashian *et al.* (unpublished).

[15]W. R. Nelson *et al.*, SLAC Report No. 265, 1985 (unpublished).
[16]Y. Doi *et al.*, Nucl. Instrum. Methods **A274**, 95 (1989).
[17]M. Gyr and C. Iselin, *Poisson Group Programs User's Guide* (CERN, Geneva, Switzerland, 1976).
[18]H. Asakura *et al.*, Rep. Faculty Sci. Eng. Saga Univ. **16**, 101 (1988).
[19]The visible energy $E_{\rm vis}$ is defined as the sum of the aboslute value of the momenta of all of the charged particles plus the energies of all the showers not associated with charged tracks.
[20]The momentum imbalance along the beam direction is defined as the sum of the z components of the three-momenta for all charged tracks and neutral showers.
[21]T. Sjöstrand and M. Bengtsson, Comput. Phys. Commun. **43**, 367 (1987).
[22]F. A. Berends, R. Kleiss, and S. Jadach, Nucl. Phys. **202**, 63 (1982); Comput. Phys. Commun. **29**, 185 (1983).
[23]G. Altarelli and G. Parisi, Nucl. Phys. **B126**, 298 (1977).
[24]B. Andersson *et al.*, Phys. Rep. **97**, 33 (1983).
[25]AMY Collaboration, Y. K. Li *et al.*, Phys. Rev. D **41**, 2675 (1990).
[26]AMY Collaboration, H. W. Zheng *et al.* (unpublished).
[27]J. Fujimoto and Y. Shimizu, Mod. Phys. Lett. A **3**, 581 (1988).
[28]A. Grant, Nucl. Instrum. Methods **131**, 167 (1975).
[29]K. Kato and T. Munehisa, KEK Report No. 84-18, 1984 (unpublished).
[30]J. Smith, University of California (Davis) Report No. UCD-88-25 (unpublished).
[31]Ch. Berger and W. Wagner, Phys. Rep. **146**, 1 (1987).
[32]N. Argeaga-Romero *et al.*, Z. Phys. C **32**, 105 (1986).
[33]In the previous paper (Ref. 2) we quote a smaller value of 0.9% for the difference between the FS (Ref. 27) and BKJ (Ref. 22) radiative corrections at $\sqrt{s}=57$ GeV. This difference was determined by compairing results from BKJ, as implemented in the LUND 63 (Ref. 21) program using the default values $M_Z=94$ GeV/c^2 and $\sin^2\theta_W=0.217$ and neglecting final-state radiation, with FS results that include final-state radiation and using $M_Z=92$ GeV/c^2 and $\sin^2\theta_W=0.230$. If we compare the BKJ results directly with those from FS, using the same values for M_Z, $\sin^2\theta_W$, and the quark masses (although still neglecting final-state radiation in BKJ), the difference is 2.5% and 3.3% at $\sqrt{s}=57$ and 60 GeV, respectively.
[34]S. Kawabata, Comput. Phys. Commun. **41**, 127 (1986).
[35]J. Fujimoto, M. Igarashi, and Y. Shimizu, Prog. Theor. Phys. **77**, 118 (1987).
[36]K. Tobimatsu and Y. Shimizu, Prog. Theor. Phys. **74**, 567 (1985).
[37]T. Sjöstrand, Comput. Phys. Commun. **39**, 347 (1986).
[38]CELLO Collaboration, H.-J. Behrend *et al.*, Phys. Lett. B **183**, 400 (1987).
[39]JADE Collaboration, W. Bartel *et al.*, Phys. Lett. **129B**, 145 (1983); Mark J Collaboration, B. Adeva *et al.*, Phys. Rev. Lett. **50**, 799 (1983); TASSO Collaboration, R. Brandelik *et al.*, Phys. Lett. **113B**, 499 (1982); MAC Collaboration, E. Fernandez *et al.*, Phys. Rev. D **31**, 1537 (1983); HRS Collaboration, D. Bender *et al.*, *ibid.* **31**, 1 (1983); L. Criegee and G. Knies, Phys. Rep. **83**, 153 (1982).
[40]CELLO Collaboration, R. Giles *et al.*, Phys. Rev. D **29**, 1285 (1984); CUSB Collaboration, E. Rice, Ph.D. thesis, Columbia University, 1982; DASP2 Collaboration, S. Weseler, Diploma thesis, University of Heidelberg, 1981; DASP2 Collaboration, H. Albrecht *et al.*, Phys. Lett. **116B**, 383 (1982). DESY-Hamburg-MPI Munich Collaboration, P. Boch *et al.*, Z. Phys. C **6**, 125 (1980); LENA Collaboration, B. Niczyporuk *et al.*, *ibid.* **15**, 299 (1982); PLUTO Collaboration, C. Berger *et al.*, Phys. Lett. **81B**, 410 (1979); Ch. Gerke, Dissertation, University of Hamburg, 1979.
[41]G. S. Gorishny, A. L. Kataev, and S. A. Larin, Phys. Lett. B **212**, 238 (1988).

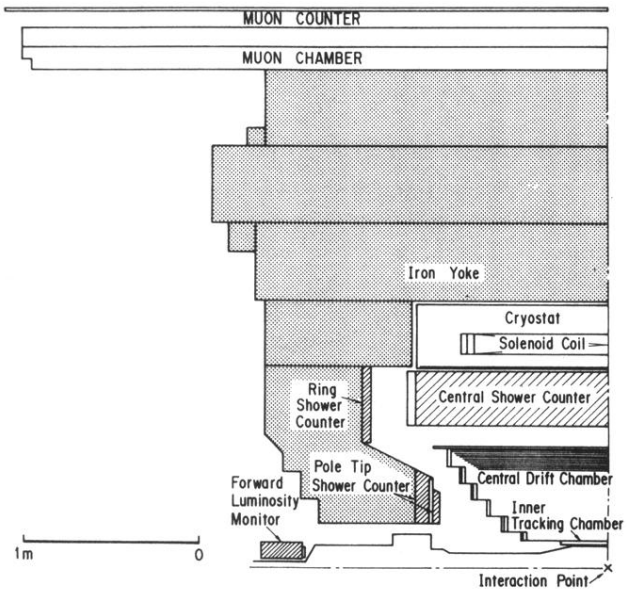

FIG. 2. A schematic view of the AMY detector.